Magnetic and Photoresponsive Theranosomes: Translating Cell-Released Vesicles into Smart Nanovectors for Cancer Therapy

Amanda K. A. Silva,[†] Jelena Kolosnjaj-Tabi,[†,‡] Stephanie Bonneau,[§] Iris Marangon,[†] Nicole Boggetto,[⊥] Kelly Aubertin,[†] Olivier Clément,[‡] Michel Francis Bureau,[∥] Nathalie Luciani,[†] Florence Gazeau,[†] and Claire Wilhelm[†,*]

[†]Laboratoire Matière et Systèmes Complexes, UMR 7057, CNRS and Université Paris Diderot, 10 Rue Alice Domon et Léonie Duquet, 75205 Paris Cedex 13, France, [‡]INSERM U970, Paris Cardiovascular Research Center-PARCC/Université Paris-Descartes, 56 Rue Leblanc, 75737 Paris Cedex 15, France, [§]Laboratoire Jean Perrin-CNRS FRE3231, Université Pierre et Marie Curie, Paris 6, Case Courrier 114, 4 Place Jussieu, 75252 Paris Cedex 05, France, [⊥]ImagoSeine BioImaging Core Facility, Institut Jacques Monod, CNRS/Université Paris Diderot, PRES Sorbonne-Paris Cité, 75205 Paris Cedex 13, France, and [∥]Unité de Pharmacologie Chimique et Génétique, CNRS, UMR 8151, Paris, F-75270 Cedex France; Inserm, U1022, Paris, F-75270 Cedex France; and Faculté des Sciences Pharmaceutiques et Biologiques, Université Paris Descartes, Paris, F-75270 Cedex, France

ABSTRACT Cell-released vesicles are natural carriers that circulate in body fluids and transport biological agents to distal cells. As nature uses vesicles in cell communication to promote tumor progression, we propose to harness their unique properties and exploit these biogenic carriers as Trojan horses to deliver therapeutic payloads to cancer cells. In a theranostic approach, cell-released vesicles were engineered by a top-down procedure from precursor cells, previously loaded with a photosensitizer and magnetic nanoparticles. The double exogenous cargo provided vesicles with magnetic and optical responsiveness allowing therapeutic and imaging functions. This new class of cell-derived smart nanovectors was named "theranosomes". Theranosomes enabled efficient photodynamic tumor therapy in a murine cancer model *in vivo*. Moreover the distribution of this biogenic vector could be monitored by dual-mode imaging, combining fluorescence and MRI. This study reports the first success in translating a cell communication mediator into a smart theranostic nanovector.

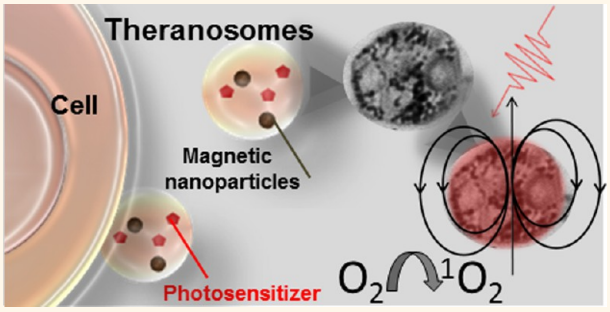

KEYWORDS: cell-derived vesicles · magnetic nanoparticles · photosensitizer · cancer · intercellular communication · theranostics

Handling organism barriers and self-defense is a major challenge in nanomedicine.[1] Synthetic vectors such as liposomes and polymeric nanoparticles are increasingly developed for drug delivery, but their comprehensive adaptability to a biological environment is still not controlled.[2] Various drug formulation strategies aim to improve the biocompatibility of drug delivery platforms, protect the therapeutic payload from degradation, delay uptake by the reticuloendothelial system,[3] enhance the crossing of biological barriers, and efficiently transfer the drug to the target. However, apart from this man-made approach, it was recently highlighted that nature possesses its own internal delivery system, which allows different biological effectors to be transported from cell to cell.[4] Naturally occurring cell vesicles, released under physiological conditions as well as in response to a variety of stimuli, indeed freely circulate in the organism.[5,6] They are nowadays regarded as biological conveyors of cellular materials participating in distal information transfer between cells.[4,7] Their implication in diverse pathophysiological processes, most notably in inflammation and cancer, is related to their unique ability to propagate biological signals stemming from parental cells and to target recipient cells. Remarkably, the endogenous properties of cell-released vesicles, in terms of membrane composition and structure, morphology, size distribution, biophysical characteristics, and internal payloads, make them unique natural vectors for intercellular communication. More explicitly, biogenic

* Address correspondence to claire.wilhelm@univ-paris-diderot.fr.

Received for review January 18, 2013 and accepted May 4, 2013.

Published online May 05, 2013
10.1021/nn400269x

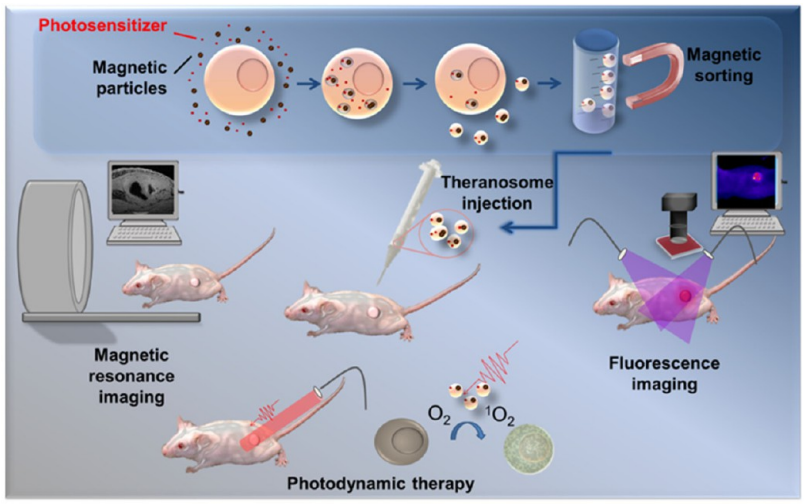

Scheme 1. Schematic representation of theranosome production from drug-loaded magnetic precursor cells and their application for photodynamic therapy and dual-mode MRI and fluorescence imaging.

vectors present highly optimized functions *in vivo*, such as natural stability in blood circulation, immunotolerance,[8] natural targeting properties, and the capacity to facilitate cell entry.[9] Moreover, most cell−material interactions are mediated by the cell membrane. In this regard, designing a therapeutic vector with cellular origin may represent a challenging opportunity for drug delivery. Exosomes, the smallest subsets of cell-derived vesicles, have been first engineered for gene or drug delivery. Purified exosomes were electroporated in order to encapsulate short interfering (si)RNA for Alzheimer's disease treatment.[10] Moreover, exosomes loaded with curcumin by hydrophobic interactions were tested in a septic shock mouse model.[11] Here we propose an alternative approach, following a top-down procedure, in which cells serve as fabrication units to produce submicrometer vesicles with specific exogenous cargoes. Our strategy aimed at exploiting the inherent properties of cellular vesicles in order to design a new generation of multifunctional theranostic vectors. For this purpose, the parent cells were first engineered to enclose both iron oxide nanoparticles and a therapeutic drug. Then they were stimulated to generate nanovesicles laden with both payloads. These cellular carriers were named "theranosomes" in regard to their combination of therapeutic and imaging properties (Scheme 1). Indeed iron oxide nanoparticles are responsive to magnetic field, allowing multiple functionalities such as magnetic manipulation, remote heating,[12,13] and tracking by magnetic resonance imaging (MRI).[14,15] Besides, the drug employed, a photosensitizer named m-THPC, is clinically used and has been reported to be one of the most active photosensitizers for photodynamic therapy (PDT).[16] In addition to singlet oxygen production, photosensitizers emit fluorescence, which enables both detection and imaging of the drug. Yet, the therapeutic outcome of PDT is currently weakened by suboptimal concentration at the tumor site and side effects related to unspecific intake in healthy tissue. Additionally, direct administration of most photosensitizers such as m-THPC suffers important limitations related to high hydrophobicity and subsequent concentration-dependent aggregation in aqueous media. Here the cellular membrane of cell-shed vesicles is expected to act as a support carrier for the hydrophobic m-THPC drug, while the magnetic nanoparticles provide MR detectability and allow magnetic manipulations of such natural therapeutic nanovectors. Our study reports the first proof of principle of designing cell-derived multifunctional nanovectors, named theranosomes, with applicability in cancer therapy.

RESULTS

Theranosome Production with Magnetic and Therapeutic Cargo. The first step in theranosome production involved an initial loading of parent cells with magnetic nanoparticles and photosensitizer. Human macrophages, derived from the monocytic THP1 cell line, were incubated with 8 nm citrate-coated iron oxide nanoparticles together with the m-THPC photosensitizer in RPMI culture medium, at a concentration below the onset of m-THPC aggregation. These nanoparticles enter the cell by adsorptive endocytosis as previously described.[17,18] Cellular internalization of nanoparticles and efficient uptake of the photosensitizer were quantified, corresponding to 30 pg of iron and 18 fmol of m-THPC per cell, respectively. To induce vesicle release, the parent cells were subsequently cultured in serum-free medium for two days. Membrane vesicles shed in the extracellular medium were then sorted overnight on a strong magnet, in order to select the vesicles loaded with iron oxide nanoparticles (Supplementary Figure 1). Transmission electron microscopy (TEM) confirmed the isolation of membrane-bound vesicles, most of them containing iron oxide nanoparticles in their internal compartment. A mean vesicle size of 332 ± 94 nm (n = 30) was

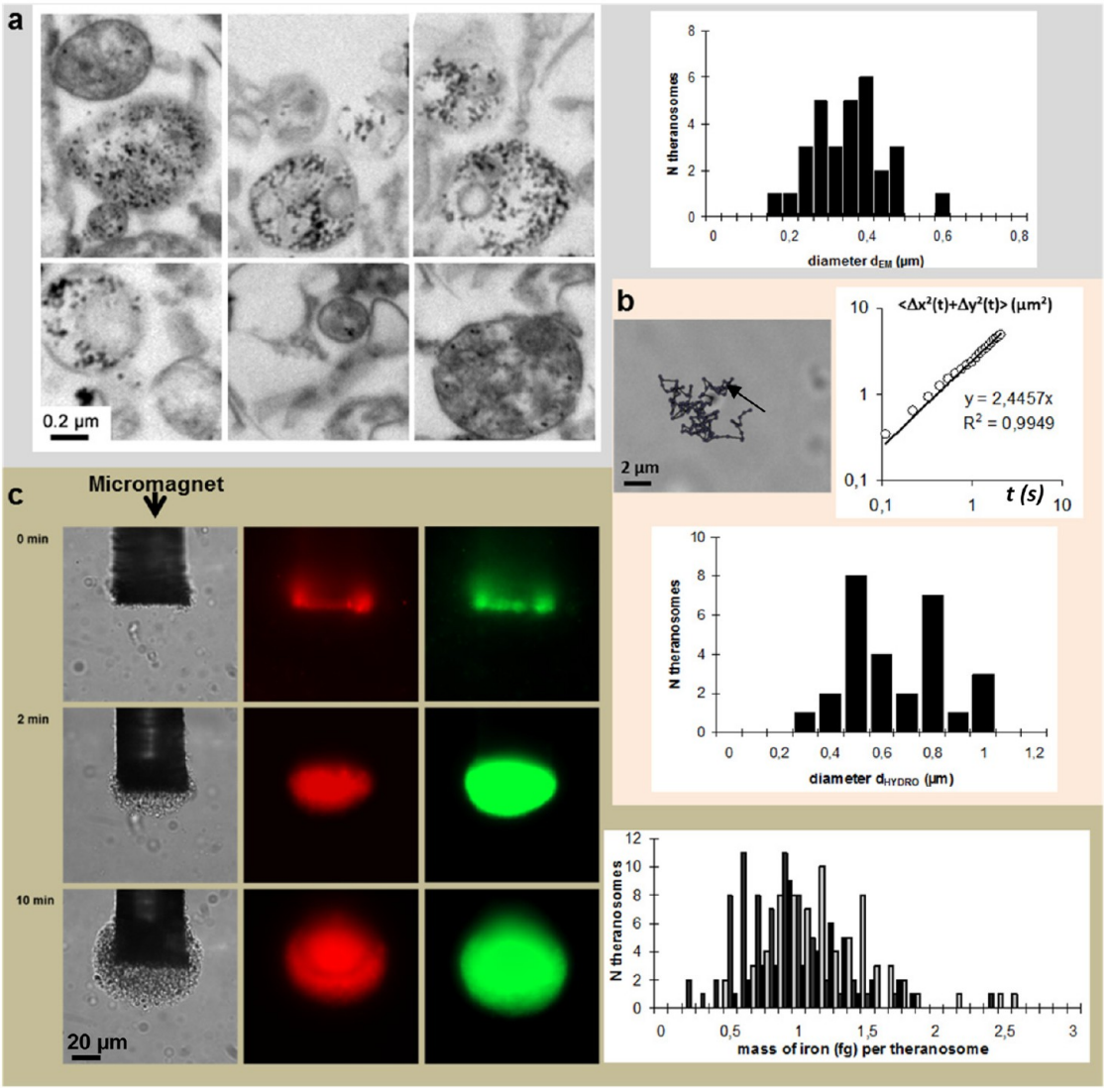

Figure 1. Characterization of theranosomes: size, magnetophoretic mobility, constitution, and iron load. (a) On the left: electron micrographs of theranosomes enclosing iron oxide nanoparticles in their core. On the right: histogram of theranosome size distribution. (b) On the upper left: optical microscopy follow-up of the Brownian motion of theranosomes. The arrow indicates the initial position of the theranosome, and the trajectories are graphically represented by interconnected dots, which indicate successive time points taken at intervals of 109 ms. On the left: random displacement of theranosomes was recorded and their diffusion coefficient D was measured from the displacements $(x(t),y(t))$ in the coordinates x and y at time t, using $\langle \Delta x^2(t) + \Delta y^2(t) \rangle = 4D\Delta t$, where brackets denote averaging over time. On the bottom: histogram of theranosome hydrodynamic size distribution calculated from the Brownian motion. (c) On the left: time series images (bright field and fluorescence) of theranosomes in the presence of a micromagnet. Red fluorescence emission from theranosomes is due to the encapsulation of the fluorescent drug m-THPC, while green fluorescence emission is the signature of the biological membrane. Theranosome detection in green (membrane) and red (photosensitizer) attests co-localization of magnetic and drug payloads within cell-derived vesicles. On the right: histogram of theranosome iron load distribution. Trajectories of theranosomes moving toward the micromagnet tip were recorded and analyzed in order to determine the theranosome magnetophoretic mobility and iron load distribution.

derived from electron micrographs (Figure 1a). Besides, the dynamical observation of the Brownian motion of single vesicles (Figure 1b) and a dynamic light scattering (DLS) experiment allowed deducing a mean hydrodynamic diameter of 610 ± 200 nm and 550 ± 50 nm, respectively. Size distribution was not changed by freezing/defrosting cycles. There was no statistically significant difference in mean hydrodynamic size determined by DLS after one, two, or three freezing/defrosting cycles ($p > 0.9$).

The co-localization of the magnetic and photosensitizer payloads within the biogenic vesicles was demonstrated through a micromagnetophoresis experiment (Figure 1c). The vesicles that moved toward the micromagnet and accumulated on it due to their magnetic payload also showed red fluorescence stemming from the photosensitizer, which was further confirmed by fluorescence spectroscopy detection (Supplementary Figure 2). In addition, the presence of a cellular membrane was confirmed by the emission

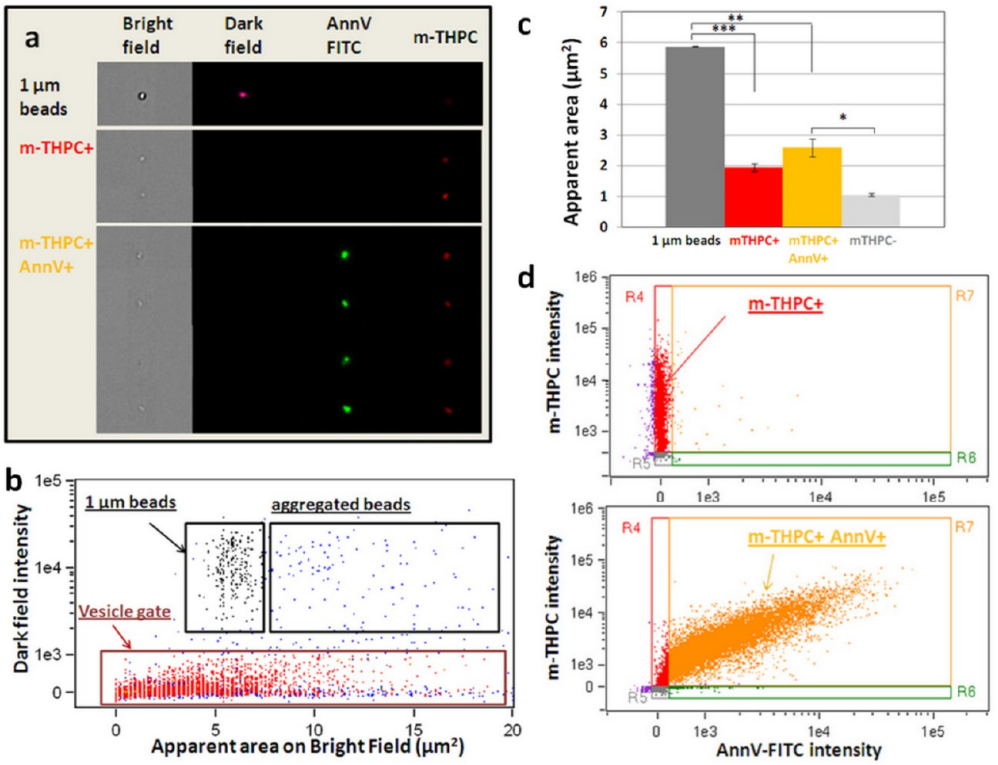

Figure 2. Vizualization and quantification of individual theranosomes by multispectral imaging flow cytometry. (a) Images acquired in four different channels (bright field, dark field, FITC green fluorescence, and m-THPC red fluorescence) were compared for specific detection of vesicles containing the red fluorescent photosensitizer: m-THPC (*m-THPC+* events). Calibration beads of 1 μm diameter were used as a size standard on the bright field image. Beads are characterized by their size, high circularity, and high intensity on the dark field images. In contrast, vesicles exhibit dim intensity on dark field images, but intense red fluorescence. When incubated with annexin V−FITC, the red fluorescent vesicles become also green fluorescent (*m-THPC+/annV+* positive events), which demonstrates the exposure of phosphatidylserine on theranosomes. (b) To distinguish vesicles and impurities from 1 μm beads, a biparametric dot plot of the dark field intensity *versus* the area on the bright field image was constructed. Calibration beads are gated in the black window. Events with both large bright field area and high dark field intensity correspond to aggregates of beads. In contrast, vesicles and buffer impurities are gated in the brown window: they are characterized by low dark field intensity. Vesicles containing m-THPC (red points on the graph) are specifically detected through their red fluorescence. The distribution of their apparent area on the bright image is larger than that of the 1 μm beads, but shifted toward lower areas. (c) The mean apparent area of m-THPC-loaded vesicles (before and after incubation with annexin V) measured on the bright field images is significantly lower than that of the 1 μm calibration beads. In contrast, nonfluorescent events show an even smaller mean area. (d) Biparametric dot plot of m-THPC fluorescence *versus* annexin V−FITC fluorescence in the absence (top) and in the presence of annexin V (bottom). 96 ± 1.5% of m-THPC positive vesicles show green fluorescence beyond the control when incubated with annexin V. For each sample, about 10 000 focused events were collected and quantified. Bar graph represents mean ± SEM from three independent preparations. *, **, and * indicate $p < 0.05$, $p < 0.01$, and $p < 0.001$, respectively.**

of green fluorescence. Indeed, green-fluorescent magnetic vesicles were obtained from macrophages whose membrane was previously stained with the membrane green marker PKH67 (Supplementary Figure 3). The monitoring of a single vesicle trajectory toward the micromagnet allowed the measurement of a magnetic mobility in the range of 1 to 8 μm/s (mean mobility of 4.6 ± 1 μm/s) and the estimation of the iron load distribution in the vesicle population (Figure 1c). On average, the observed vesicles contained an iron mass of 1 ± 0.22 fg with a width of the distribution of 36 ± 8%. After the isolation procedure, the concentration of m-THPC was found to be 25 ± 3.6 μM for an iron concentration of 5 mM, from which a theranosome density of 3×10^8 per μL was estimated (Supplementary Figure 4).

Theranosomes Present the Hallmark of Cell Microvesicles. Cell-released vesicles were also characterized using multispectral imaging flow cytometry (Figure 2). This technique combines the statistical power of high-throughput flow cytometry with the analytical advantages of confocal microscopy on each detected event. Images of about 10 000 theranosomes per sample were collected in the bright field, dark field, and green and red fluorescence channels, simultaneously. Single vesicles containing m-THPC were readily detected through their red fluorescence (Figure 2a) and distinguished from 1 μm calibration beads by their lower side-scattered intensity (Figure 2b). In agreement with size distribution assessed on TEM and diffusion light scattering, the mean apparent area on bright field images was about 2-fold lower for the m-THPC-positive vesicles in comparison to the 1 μm beads (2.68 ± 0.29 μm^2 *versus* 5.88 ± 0.02 μm^2, $p < 0.01$). Conversely, the m-THPC-loaded vesicles were

larger than nonfluorescent events, which comprise mostly buffer impurities (2.68 ± 0.29 μm^2 *versus* 1.04 ± 0.05 μm^2, $p < 0.05$) (Figure 2c). The presence of negatively charged phosphatidylserine in the outer membrane is a general hallmark of cell-shed vesicles with size in the range of 0.1−1 μm.[19] It actually reveals the stress-induced redistribution of plasma membrane constituents, which leads to vesicle release. Incubation of theranosomes with annexin V−FITC shows that 96 ± 1.5% of the red m-THPC-loaded vesicles became green due to annexin V binding on phosphatidylserine (Figure 2d). Together with TEM and magnetophoresis, this confirms that the so-prepared theranosomes share the morphological and membrane characteristic of natural cell-released vesicles, while transporting both the drug and magnetic nanoparticles. In addition, theranosomes remained red fluorescent at least 6 months after production when stored at −20 °C or 2 months at 4 °C. This may indicate good shelf time, minimal leakage of the drug, and theranosome integrity preservation over months.

Theranosomes Transfer Therapeutic Cargo to Cancer Cells. The transfer of dual cargo from theranosomes to cancer cells was first assessed *in vitro*. TC-1 (murine cervical cancer) and PC3 (human prostate cancer) cells were treated with theranosomes dispersed in RPMI culture medium overnight and subsequently observed by TEM. Electron dense nanoparticles were observed inside recipient cancer cells. Such electron dense nanoparticles were similar to the ones enclosed within theranosomes, indicating an efficient translocation of iron oxide nanoparticles to TC-1 and PC3 cancer cells (Figure 3a). The transfer of iron oxide nanoparticles from theranosomes to TC-1, PC3, and also SKOV-3 (human ovarian cancer) cells was further confirmed by Prussian blue staining (Supplementary Figure 5). Theranosome internalization was then monitored by confocal microscopy and flow cytometry (Figure 3). Here theranosomes' green staining was systematically achieved by the initial labeling of the membrane of the precursor cells by PKH67 (Supplementary Figure 3). Confocal images of TC-1 cells incubated with theranosomes for 2 or 18 h are shown in Figure 3b. For both conditions, diffuse red fluorescence emission from m-THPC drug (left) was observed, while the membrane green staining exhibited a spot-like localization (middle). In order to statistically quantify the intracellular theranosomes' delivery, multispectral imaging flow cytometry was then carried out. TC-1 cells were incubated for 18 h with PKH67-stained theranosomes (condition m-THPC/PKH67 vesicles), theranosomes (m-THPC vesicles), PKH67 vesicles nonloaded with m-THPC (pkh67 vesicles), or vesicle-free culture medium (negative control). For each condition, 10^4 cells were imaged in the bright field, dark field, and blue, green, and red fluorescence channels, simultaneously. The condition corresponding to incubation with the PKH67-stained theranosomes presented green fluorescence from the PKH67-stained membrane of theranosomes as well as red fluorescence from the theranosome drug payload (Figure 3c). Most events (84.3%) were positive for both m-THPC and PKH67 (Figure 3d and e), which indicates that m-THPC uptake took place to a very significant extent and that it was mediated by theranosomes. Conversely, only red or green fluorescence was observed for the incubation condition with unlabeled theranosomes (m-THPC vesicles) or PKH67 vesicles, respectively, while no red or green fluorescence was detected after incubation with vesicle-free culture medium (negative control) (Supplementary Figure 7a and b). Similarly to confocal images, red fluorescence was always observed widespread in the cytoplasm, while green fluorescence was characterized by focal spots. This further suggests m-THPC release from theranosomes confined in endosomal/lysosomal compartments.

In fact, m-THPC is a hydrophobic molecule able to diffusely redistribute throughout the cytoplasm once internalized. The characteristic diffuse pattern of m-THPC intracellular localization in cells incubated with free m-THPC in solution can be observed in Supplementary Figure 6. The same cytoplasmic redistribution was observed after theranosome uptake. The redistribution of m-THPC from the vesicles to the cytosol is of particular importance for the treatment efficiency. Actually, PDT generates toxic reactive oxygen species whose lifespan is very short so that their action is highly localized and would be impaired by an endosomal localization for reaching the intracellular targets, for instance mitochondria for m-THPC.[16] Therefore, the cytoplasmic redistribution of m-THPC vectorized by theranosomes, in a pattern similar to that of m-THPC free in solution, is indeed quite advantageous and essential.

Drug uptake in TC-1, PC3, and SKOV-3 cells after incubation of two hours with theranosomes or m-THPC (both dispersed in RPMI) was compared (Figure 3f). Theranosomes could efficiently transport the drug and deliver it to three cancer cell types. A dose-dependent uptake was observed. The kinetics of uptake of the drug cargo was also quantitatively investigated in SKOV-3 cells by fluorescence spectroscopy (Supplementary Figure 8).

Theranosomes were well tolerated *in vitro*, as demonstrated by the Alamar Blue viability test, assessing metabolic activity (Supplementary Figure 9a). There were no changes in cell morphology or adhesion (Supplementary Figure 9b). The therapeutic effect was examined after light exposure, which activated the photosensitizer payload (Figure 3g). Theranosomes presented a marked light toxicity in a concentration-dependent manner, compared to the nonirradiated control. In addition, theranosome-mediated delivery and m-THPC treatment achieved comparable reduction of

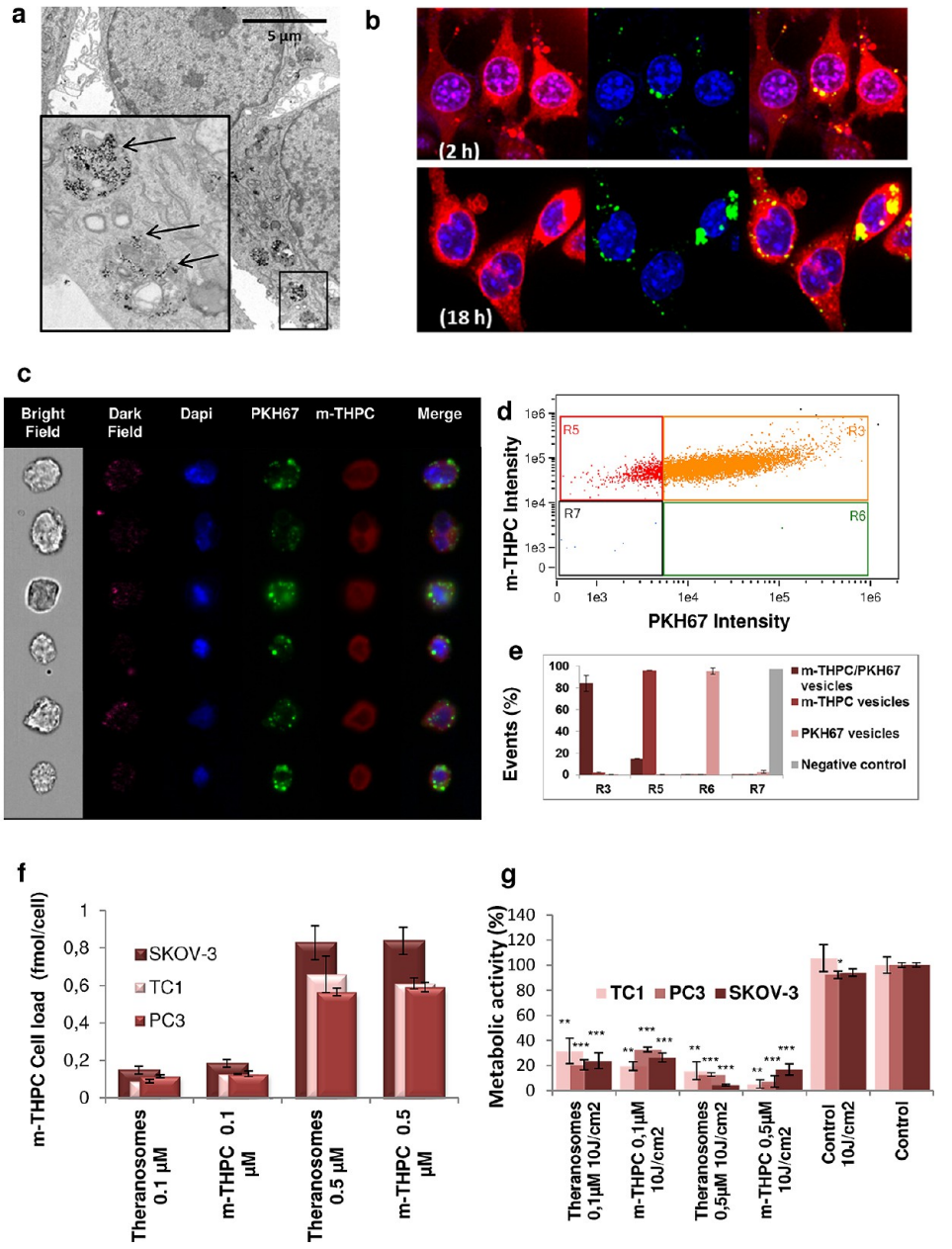

Figure 3. *In vitro* translocation of theranosome dual cargo into cancer recipient cells and theranosome-mediated therapeutic effect. (a) Electron micrograph of TC-1 cancer cells after incubation with theranosomes. The endosomal internalization of iron oxide nanoparticles is evidenced in the inset. (b) Confocal microscopy of TC-1 cancer cells after theranosome incubation. The upper line represents a 2 h incubation condition, while the lower line illustrates a 18 h incubation condition: red fluorescence is emitted from m-THPC, blue fluorescence from Dapi nucleus staining, and green fluorescence from theranosome membrane staining with PKH67. Overlaps of m-THPC and Dapi (left); PKH67 and Dapi (middle); m-THPC, PKH67, and Dapi (right) are presented. (c) ImageStream multispectral imaging flow cytometry of theranosome internalization in tumor TC-1 cells. TC-1 cells were incubated for 18 h with PKH67-stained theranosomes. Images were acquired in five different channels (bright field, dark field, Dapi blue fluorescence, PKH67 green fluorescence, and m-THPC red fluorescence) and were compared for specific detection of cells containing both the red fluorescent photosensitizer m-THPC (m-THPC+ events) and the green fluorescent PKH67 from theranosome membrane (PKH+ events). (d) Biparametric dot plot of m-THPC fluorescence *versus* PKH67 green fluorescence of TC-1 cells 18 h after incubation with PKH67-stained theranosomes. (e) Percentage of cell events per gate corresponding to cells positive to either both m-THPC and PKH67 (R3), m-THPC only (R5), PKH67 only (R6), or none (R7). The different conditions correspond to PC-1 cells incubated with either theranosome vesicles loaded with m-THPC and stained with PKH67 (m-THPC/PKH67 vesicles), theranosome vesicles loaded with m-THPC with no membrane staining (m-THPC vesicles), vesicles stained with PKH67 but nonloaded with m-THPC (PKH67 vesicles), or vesicle-free culture medium (negative control). (f) m-THPC uptake by TC-1, PC3, and SKOV-3 cells after theranosome or m-THPC incubation at 0.1 or 0.5 μM for 2 h determined by fluorescence spectroscopy. (g) Metabolic activity assessed by Alamar Blue and normalized to nontreated controls of TC-1, PC3, and SKOV-3 cells 48 h after theranosome or m-THPC incubation at 0.1 or 0.5 μM for 2 h, followed by light exposure (λ = 650 nm, 10 J/cm^2, 100 mW/cm^2 for 100 s) 20 h later. All error bars reflect SD (n = 3). *, **, and *** indicate $p < 0.05$, $p < 0.01$, and $p < 0.001$, respectively, *versus* untreated control (no incubation, no light exposure), designated as Control. The groups that were irradiated are indicated by the designation 10 J/cm^2.

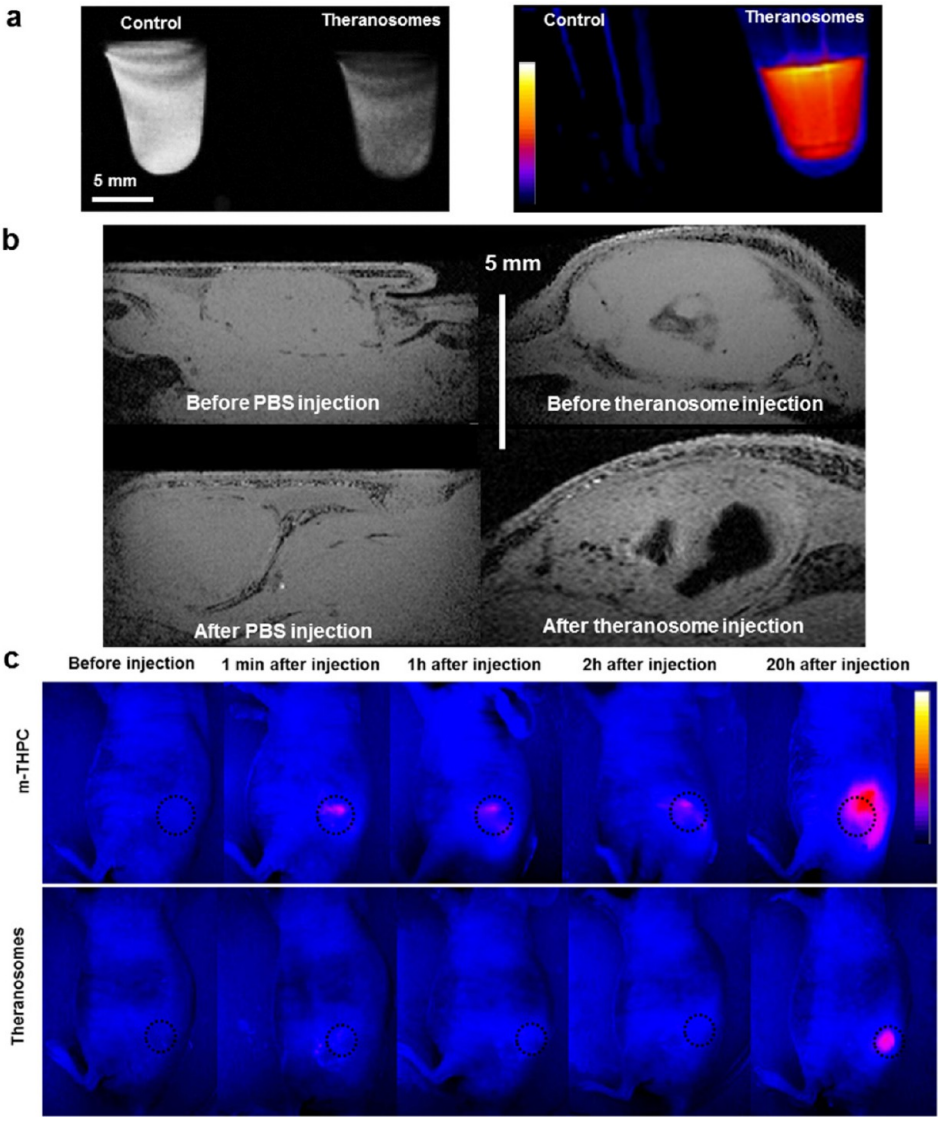

Figure 4. Theranosome dual-mode imaging *in vitro* and *in vivo* and theranosome-mediated therapeutic effect *in vivo*. (a) Dual-mode imaging of theranosomes *in vitro*. Left: T2*-weighted MRI scan of agarose alone (control) and theranosomes dispersed in agarose gel. Right: false-color image of fluorescence emission from RPMI culture medium (control) *versus* theranosomes dispersed in RPMI. (b) Left: MRI scans of TC-1 tumors before and 48 h after PBS intratumoral injection (control group). Right: MRI scans of tumors before and 48 h after theranosome intratumoral injection. (c) False-color images of fluorescence emission from nude mice bearing TC-1 tumor before and after theranosome or m-THPC intratumoral injection, as a function of time.

cell metabolic activity, which was consistent with drug uptake data.

We first investigated theranosome detectability *in vitro* by *in vivo* techniques of MRI and fluorescence imaging (Figure 4a). Agarose phantoms containing the vesicles presented marked hypointensity in a T2*-weighted MRI sequence, which was ascribed to the presence of magnetic nanoparticles. A dilution series of theranosomes in agarose gel was prepared and analyzed by MRI (Supplementary Figure 10). Considering that detection is achieved once T2 is approximately shortened by half its intrinsic value T2° (without contrast agent), the MRI detection limit for theranosomes was about 4×10^6 theranosomes/μL (Supplementary Figure 10). Concerning fluorescence imaging, theranosomes showed an intense red color emission upon light excitation at 400 nm using an imaging setup designed for *in vivo* fluorescence tracking, owing to the presence of the fluorescent drug.

For the *in vivo* experiment, theranosomes or m-THPC was injected intratumorally into NMRI nude mice bearing solid subcutaneous TC-1 tumors. m-THPC at 25 μM was solubilized in ethanol/polyethylene glycol 400/water at a 2/3/5 volume ratio, while theranosomes were in RPMI medium. The concentration of m-THPC in theranosomes was also 25 μM, which represents an iron concentration of 5 mM and a theranosome density of 3×10^8 per μL. In the attempt to assess the intratumoral distribution of the dual photosensitizer/nanoparticle payload of theranosomes, MRI

and fluorescence imaging were carried out. For both techniques a high signal-to-noise ratio was obtained, providing the tracking of the theranosome dual cargo *in vivo*. On MRI scans (Figure 4b), a large zone of hypointense intratumoral signal was observed within the tumor after theranosome injection, confirming intratumoral localization of theranosomes. Conversely, such contrast changes in MR scans were not observed in tumors of the control group. Fluorescence imaging (Figure 4c) was used to track the intratumoral localization of the drug after injection. For both theranosomes and m-THPC alone, there was an important increase in fluorescence signal 20 h after injection. This may be due to m-THPC diffusion toward the tumor surface, where the photosensitizer is more efficiently excited by blue light. However, while extratumoral extravasation was observed for the free drug, theranosomes generated a signal that was restrained to the tumor site. Drug redistribution to the other organs was investigated 24 h after theranosome or m-THPC injection. No remarkable fluorescence emission could be detected in the liver, skin, lungs, spleen, kidneys, or heart, compared to control (Supplementary Figure 11).

Theranosome-Mediated *in Vivo* Cancer Therapy. This study also provided evidence of the therapeutic effect of theranosomes, considering the reduction in tumor growth during the seven days following the treatment (Figure 5a). Mice intratumorally injected with RPMI and laser irradiated; RPMI without laser irradiation; m-THPC (100 μM) in RPMI (without PEG) and laser irradiated; m-THPC (100 μM) in RPMI (without PEG) and without laser irradiation presented a tumor growth similar to laser-irradiated, non-injected control (Supplementary Figure 12) and non-irradiated and non-injected mice (Figure 5a). Theranosome treatment significantly reduced tumor growth compared to non-treated control ($p < 0.01$) at day 7. At this time point, the study was interrupted because control tumors attained the critical size imposed by the ethical committee. Theranosome-mediated effect was more important than tumor response to the m-THPC alone compared to control ($p < 0.05$). Concerning the tumor growth curve for the m-THPC group, it is interesting to point out that tumor growth at day 2 surpasses those from theranosomes and control groups. In fact, the tumor and its surroundings presented a notable swelling (Supplementary Figure 13a). This is probably related to the cytotoxic effect of the free drug that leaked in the extratumoral space, as indicated by fluorescence imaging for free m-THPC. The presence of drug in the outer periphery of the tumor extended the zone affected by photodynamic therapy while depleting the photodynamic effect at the tumor site. This may contribute to m-THPC's inferior therapeutic effect compared to theranosomes, which are more restrained at the tumor site. An improved therapeutic effect mediated by theranosome treatment compared to free m-THPC was presented in Kaplan-Mier's plot (Supplementary Figure 13b): 0% of control tumors and 40% of m-THPC tumors were under a 3-fold growth, while this value was 80% for the theranosome-treated group at day 7.

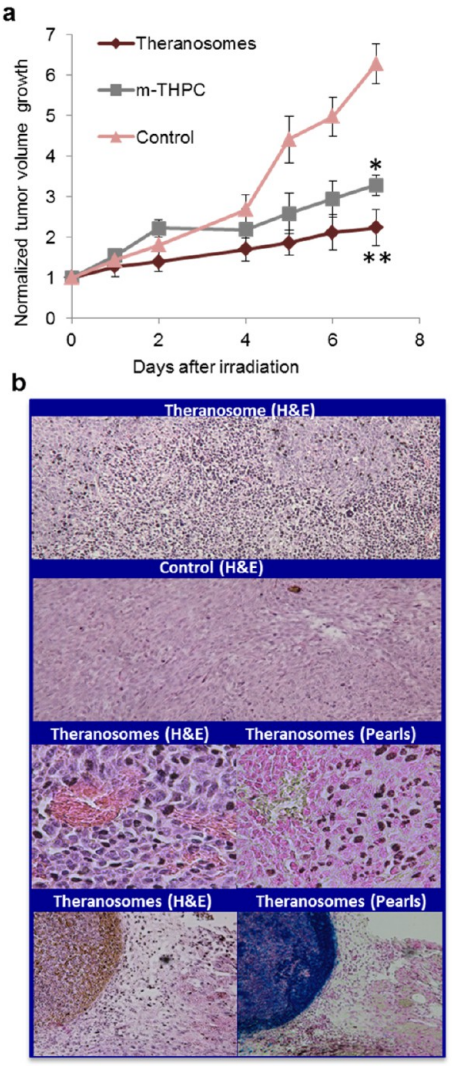

Figure 5. ***In vivo*** **theranosome-mediated therapeutic effect. (a) Tumor growth curves (tumor volume is normalized to day 0) for mice intratumorally injected with theranosomes (25 μM m-THPC concentration) or m-THPC (25 μM) both followed by light exposure (λ = 630 nm, 30 J/cm^2, 77 mW/cm^2 for 390 s) 20 h later, compared with untreated control. All error bars reflect the SEM ($n = 5$). * and ** indicate $p < 0.05$ and $p < 0.01$, respectively, *versus* untreated control (no injection of therapeutic agent, no light exposure) at day 7. The m-THPC concentration of 25 μM in theranosomes corresponds to an iron concentration of 5 mM and a theranosome density of 3 $\times$ 10^8 per mL. (b) Histological analysis of tumors. Hematoxylin–eosin (H & E) staining of theranosome-treated tumor (2 days after irradiation) presenting necrosis associated with immune cell infiltration at 100$\times$ magnification (first line) and control tumor (second line). Hemorrhagic necrosis in theranosome-treated tumor stained by H & E (third line on the left) and Perl's staining (third line on the right) at 200$\times$ magnification. Presence of iron in theranosome-treated tumors visualized as brown areas in H & E (fourth line on the left) and blue ones after Perl's staining (fourth line on the right) both at 100$\times$ magnification.**

Histological analysis (Figure 5b) of theranosome-treated tumors after hematoxylin–eosin (H & E) staining revealed necrosis associated with immune cell infiltration (Figure 5b, fist line, and Supplementary Figure 14) compared to the control (Figure 5b, second line, and Supplementary Figure 15) or hemorrhagic necrosis (Figure 5b, third line and Supplementary Figure 16). The presence of iron within the tumors was observed as a brownish color in H & E staining (Figure 5b, fourth line on the left) and confirmed with Perl's staining (Figure 5b, fourth line on the right), confirming MRI data. Blue spots characteristic of the presence of iron were observed in the cytoplasm of cells in the tumor site after mice were treated with theranosomes (Supplementary Figure 17). No characteristic blue staining was observed for the control group (Supplementary Figure 8).

DISCUSSION

Theranosome therapeutic effect, as evidenced by tumor growth curves and histological examination, may rely on the vehicle intrinsic features, which are in line with the active role of cell-derived vesicles in cancer cell cross-talk. It is important to emphasize that during the course of tumor survival and progression malignant cells actively communicate through continuous release of vesicles. These are transferred throughout the cancer cell population and also to stromal cells and endothelial cells. Cancer cells use vesicles to their own advantage to induce the acquisition of aggressive phenotype[20] and promote invasiveness,[21] angiogenesis,[22,23] immune escape,[24,25] and drug resistance.[26,27] Some reports evidenced the receptiveness of cancer cells to interact with vesicles released from nonmalignant cells. For instance, vesicles released from fibroblasts were found to interact with cancer cells and stimulate their migration.[28] It was also observed that platelet-derived vesicles were taken up by different cancer cell lines, transferring the platelet-derived surface receptors.[29,30] Indeed, noncancer cell receptors were identified in vesicles originated from cancer cells. For instance, circulating vesicles from metastatic cancer patients coexpressed platelet-exclusive antigen CD61 and the cancer cell marker MUC1.[31] It has been suggested that cancer cell ability to fuse with vesicles derived from noncancer cells would represent a mechanism of camouflage.[32] The acquisition of lipids and membrane-specific proteins of nontransformed cells could facilitate cancer cell escape from the immune system.

Considering the importance of vesicle-mediated communication for cancer cells, our approach crosses the boundaries of material science and cell biology to translate naturally occurring vesicles into intrinsically biocompatible bioinspired theranostic nanovectors for cancer therapy. Actually, ongoing efforts have focused on combining therapy and imaging in a single synthetic platform,[33,34] that is, for instance, the case of liposome–nanoparticle hybrids.[35] In contrast, our study explored, for the first time, how cell-released conveyors could act against cancer cells by delivering a theranostic cargo. We have proposed an unprecedented procedure to engineer biogenic cellular nanovectors endowed with both dual-imaging and therapeutic properties. The cellular membrane of vesicles was used to carry a hydrophobic clinically approved photosensitizer, while magnetic nanoparticles were in the inner core. As proof of principle, we demonstrated that cancer cells are receptive to our magnetic and photoresponsive biogenic theranosomes both *in vitro* and *in vivo*. Their cargo was successfully transferred to malignant cells and induced tumor regression after light exposure. Image-guided therapy was also achieved by combined MRI and fluorescence imaging of the drug and magnetic payloads of theranosomes. Indeed, this study established a proof of principle of theranosome potential for imaging and therapy. However, in order to go further and gain insight in the translational potential of our approach, systemic administration must be addressed. We expect that theranosomes will be able to circulate in the organism without massive uptake by the RES. By virtue of their unique constitution, they may not be recognized as exogenous particles and their cell-like shell may favor interaction with cells, especially cancer cells, that present high receptiveness to cell-released vesicles, as discussed above.

Considering some aspects, cell-released vesicles are similar to liposomes. Their similarities and differences are an important point to be considered. Liposomes are spherical, closed structures, composed of curved lipid bilayers, which enclose an aqueous medium in their interior. The same applies to cell-released vesicles except that vesicles also present proteins in their membrane and other biomolecules in the inner aqueous core that stem from the precursor cell. The size of a liposome ranges from 20 nm up to several micrometers, while vesicle size ranges from 100 nm to 1 μm. Liposomes and cell-released vesicles can encapsulate molecules with different solubilities. While hydrophobic molecules can localize in the membrane, hydrophilic ones can be carried into the inner core. There was a long road from when liposomes were first synthesized in the 1960s until translation to clinics succeeded.[36,37] The structural similarities of the presented vesicles to liposomes seem to indicate that these biogenic analogues may accomplish the same achievements in the future. However, it should be considered that differently from liposomes, cell microvesicles may be recognized as self-structures. They have in fact the intrinsic vocation to ferry endogenic material and chaperone it to other cells. They are natural effectors of intercellular communication, acting as natural endogenous vectors.[4,7] Translating cell microvesicles into

carriers of an exogenous payload, as demonstrated herein, opens up new perspectives. Nevertheless, the complexity of vesicles related to their natural origin should be thoroughly addressed in order to control and appropriately take advantage of the unique features of cell-released vesicles for the design of a bioinspired biomimetic vector.

CONCLUSIONS

Herein, cell-released vesicles were engineered by a top-down procedure from precursor cells in order to enable loading with a photosensitizer and magnetic nanoparticles. The double exogenous cargo provided vesicles with magnetic and optical responsiveness, allowing therapeutic and imaging functions. These cell-derived smart nanovectors, named theranosomes, were exploited as Trojan horses to deliver therapeutic payloads to cancer cells. Theranosomes enabled efficient photodynamic tumor therapy in a murine cancer model *in vivo*. Moreover, the distribution of this biogenic vector could be monitored by dual-mode imaging, combining fluorescence and MRI. In perspective, theranosome production, based on modified cells as fabrication units, might be scaled up using bioreactors. This confers a high versatility to our approach, enabling a potential high-throughput production of theranosomes. Additionally, the procedure could be applied virtually to any cell type. Such vectors could be therefore provided with specific targeting properties, inherited from precursor cells and immunotolerance, in the case of self-derived vesicles. Nevertheless these key advantages of the biogenic nature of theranosomes have yet to be fully assessed. A better understanding of the role of cellular vesicles in pathology, in conjunction with advanced nanotechnology tools, may pave the way toward a new generation of drug delivery systems inspired by nature.

EXPERIMENTAL SECTION

Cell Culture. The human myelo-monocytic THP-1 cell line at a density of 0.2×10^6 to 1×10^6 cells/mL was cultured in suspension in RPMI 1640 medium supplemented with 10% (v/v) fetal bovine serum, 100 U/mL penicillin−streptomycin, and 2 mM L-glutamine at 37 °C in 5% CO_2. In order to induce differentiation into macrophages, THP-1 monocytes, at a cell density of 4×10^6 cells in 5 mL of RPMI medium, were treated with phorbol ester (phorbol 12-myristate 13-acetate) at a concentration of 50 ng/mL during 7 days. The TC-1 cells were cultured in RPMI 1640 medium supplemented with 10% (v/v) fetal bovine serum, 100 U/mL penicillin−streptomycin, 1 mM sodium pyruvate, and 2 mM L-glutamine at 37 °C in 5% CO_2. The PC3 cells were cultured in DMEM medium supplemented with 10% (v/v) fetal bovine serum, 100 U/mL penicillin−streptomycin, and 2 mM L-glutamine at 37 °C in 5% CO_2. The culture of SKOV-3 cells was performed with McCoy's medium supplemented with 10% (v/v) fetal bovine serum, 100 U/mL penicillin−streptomycin, and 2 mM L-glutamine at 37 °C in 5% CO_2.

Loading Precursor Cells with Magnetic Nanoparticles and m-THPC Drug. The THP-1 macrophages were incubated with a suspension containing 10 μM 5,10,15,20-tetra(*m*-hydroxyphenyl)-chlorin) (m-THPC), from Frontier Scientific, and citrate-coated 8 nm maghemite nanoparticles diluted at 5 mM iron concentration dispersed in serum-free RPMI medium supplemented with 5 mM sodium citrate. The THP-1 macrophages were subjected to a 2 h incubation at 37 °C. Afterward, cells were rinsed in serum-free RPMI medium and left for an overnight chase at 37 °C in order to allow nanoparticle internalization by cells. Additionally, to evidence the biogenic nature of the emitted vesicles, the dually loaded precursor cells were fluorescently labeled with PKH67 green fluorescent cell linker according to the manufacturer's instructions (Sigma) before triggering vesiculation.

Vesicle Release by Precursor Cells and Purification. In order to trigger vesicle release by dually loaded parent cells, cells were stressed by culture in serum-depleted medium for 2 days. This starvation stress results in the release of cell vesicles. Such conditioned medium was centrifuged (1125*g* during 10 min) to eliminate cells and large apoptotic bodies, and theranosomes were purified by magnetic sorting due to their magnetic cargo. The medium was placed in a 10 mL syringe and subjected to a magnetic field gradient overnight (magnetic field gradient of 55 T m^{-1}). Theranosomes underwent magnetophoresis: they migrated toward the edge of the magnet and accumulated on the syringe wall. The residual medium was removed under the magnetic field gradient, and the theranosome fraction was recovered (Supplementary Figure 1).

Transmission Electron Microscopy. Electron microscopy observations of samples consisting of theranosomes and cancer cells after theranosome incubation were carried out on a Zeiss EM 902 transmission electron microscope at 80 kV (platform MIMA2, INRA, Jouy-en-Josas, France). Samples were fixed in a 5% glutaraldehyde solution in 0.1 mol/L sodium cacodylate buffer, gradually dehydrated in ethanol, and stained with 1% osmium tetroxide and 1.5% potassium cyanoferrate. The samples were embedded in Epon and sectioned for analysis.

Hydrodynamic Size Determination from Brownian Motion. The Brownian motion of theranosomes was used to calculate their hydrodynamic size. Random displacement of theranosomes was recorded and their diffusion coefficient D was measured by computing the displacements in the coordinates x and y at time t ($x(t)$,$y(t)$) and the mean square displacement $\langle \Delta x^2(t) + \Delta y^2(t) \rangle = 4D\Delta t$, where brackets denote averaging over time. The slope ($4D$) on the graphs allows deriving the hydrodynamic diameter (d_{hydro}) of the tracked theranosome, following the Stokes−Einstein equation for diffusion of spherical particles: $D = (k_B T)/(3\pi\eta d_{hydro})$, where k_B is the Boltzmann constant, 1.38×10^{-23} m^2 kg s^{-2} K^{-1}, T the temperature in Kelvin, and η the water viscosity, 10^{-3} Pa·s.[38] Size determination was averaged over 28 independent theranosomes.

Micromagnetophoresis Experiment. The magnetophoretic velocity of theranosomes moving toward a micromagnet tip was analyzed using a previously published experimental setup.[38] In brief, magnetophoresis was observed with a 60× objective from an optical microscope (DMIRB Leica; Leica Microsystems, Wetzlar, Germany) connected to a charge-coupled device camera and a computer. Image J software was used to follow the x,y-position of each individual nanocontainer through the stack of successive frames (bright field and fluorescence) captured at regular time intervals. Magnetophoretic trajectories were used for determining theranosome iron load. In brief, determination was performed by computing the velocity of individual theranosomes moving toward the magnetic tips measured in the region 100 μm away from the tip surface (in which the corresponding magnetic field gradient is B_{grad} = 194 T/m). The magnetic moment M of the theranosomes in the applied magnetic field of 0.2 T can be determined from the magnetophoretic velocity v and the hydrodynamic diameter d_{hydro} values using the Stokes relation for the drag force, $3\pi\eta d_{hydro} v = MB_{grad}$. This magnetic moment equals on average $M = (1.5 \pm 0.3) \times 10^{-14}$ A·m^2. Finally, considering the nanoparticles' magnetization at 0.2 T (2.6×10^5 A/m) and the

nanoparticles density (4.9×10^6 g/m^3), conversion between magnetic moment and the mass of iron is $M/\text{pg} = 7.7 \times 10^{-14}$ A·m^2/pg. The distribution of the iron load per theranosome was calculated by three independent measurements, during which 70 theranosome magnetic mobilities were tracked.

Dynamic Light Scattering. The hydrodynamic size of the vesicle suspension was investigated using a Zeta Sizer (Malvern Instruments) equipped with a 4.0 mW He−Ne laser operating at 633 nm and an Avalanche photodiode detector. The Contin model was applied to obtain size data.

Multispectral Imaging Flow Cytometry. Vesicles images were acquired with the ImageStream^X multispectral imaging flow cytometer (Amnis Corporation, Seattle, WA, USA), collecting about 20 000 events per sample at 60× magnification and operating in the standard mode with a core diameter of 6 μm. Lasers of 488 and 405 nm wavelength were used to excite FITC and m-THPC dyes, respectively. The fluorescence images were collected using the 480−560 and 660−745 nm spectral detection channels, respectively. For double-stained cells (FITC and m-THPC), single-stained controls were used to compensate fluorescence between channel images on a pixel-by-pixel basis. Dark field images were acquired using a 785 nm laser. The system used 1 μm nonfluorescent speed beads (calibration SpeedBeads, Amnis) that are continuously run through the flow during the operation of the ImageStream^X. Vesicles obtained from cells labeled only with magnetic nanoparticles were used as nonfluorescent control. To test the presence of phosphatidylserine on vesicles, 30 μL of sample was suspended in 30 μL of binding buffer and incubated with 1.2 μL of annexin V−FITC conjugate in the presence of calcium (5 mM $CaCl_2$) at room temperature for 10 min protected from light according to the manufacturer's protocol (Sigma-Aldrich, Saint-Quentin Fallavier, France). Images were analyzed using IDEAS image-analysis software (Amnis). Events within the focal plane were selected by using a threshold on the RMS gradient feature on the bright field images. Focused events represented about 50% of the total number of events.

For imaging of the labeled cells, TC-1 cells were incubated for 18 h with PKH67-stained theranosomes (condition m-THPC/PKH67 vesicles), theranosomes (m-THPC vesicles), PKH67 vesicles nonloaded with m-THPC (pkh67 vesicles), or vesicle-free culture medium (negative control). For each condition, 10^4 cells were imaged in the bright field and dark field as well as blue, green, and red fluorescence channels in order to detect Dapi, PKH67, and m-THPC, respectively. A biparametric dot plot of m-THPC fluorescence *versus* PKH67 green fluorescence of TC-1 cells was set for each experimental group. According to the fluorescence emission profile, events were distributed in gates corresponding to cells positive to either both m-THPC and PKH67 (R3), m-THPC only (R5), PKH67 only (R6), or none (R7).

Magnetic Resonance Imaging (MRI). The MRI was performed on a 4.7 T preclinical MRI scanner (BioSpec 47/40 USR, Bruker). High-resolution MRI was performed with a cryogenic probe (Cryoprobe, Bruker). The MRI phantom gels were prepared either with 0.3% low-melting-point agarose alone or agarose spiked with theranosomes. Scans were run under a fast imaging with steady-state precession (FISP) protocol on free induction decay (FID) mode. Images were acquired with the following parameters: FOV of 15 mm × 6 mm; acquisition matrix of 150 × 300; voxel of 50 × 50 × 50 μm^3; echo time of 5 ms; repetition time of 20 ms; flip angle of 25°; and pixel bandwidth of 166 Hz.

Fluorescence Imaging. Real-time fluorescence imaging was performed with an Apogee ALTAU47 CCD camera, which is based on planar reflection fluorescence. Tube samples or animals were exposed to blue filtered light (400 ± 25 nm). Fluorescence emission was detected above 600 nm using a high-pass filter. On the given color image, reflection of the excitation light (blue) was not suppressed, but that did not alter fluorescent light, which is far from excitation light. Images were treated using Macbiophotonics ImageJ software.

Theranosome-Mediated Drug Uptake and Cytotoxicity Assessment. The PC3, SKOV-3, and TC-1 cells were seeded in 24-well plates and incubated overnight at 37 °C in a humidified 5% CO_2 atmosphere. After PBS rinsing, the cells were incubated with 250 μL of theranosomes or m-THPC at 0.1 or 0.5 μM during 30 min, 2 h, 6 h, or 24 h in the dark at 37 °C in a humidified 5% CO_2 atmosphere. After that, cells were rinsed, and part of them lysed using Triton X-100 solution (0.3% final concentration) for quantification of drug uptake by fluorescence spectroscopy. The other cell fraction was incubated for 24 h. Cells were observed by an optical microscope (Leica, Germany), and their metabolic activity was assessed by the Alamar Blue test (Invitrogen), according to the supplier's instructions.

m-THPC Quantification. The concentration of m-THPC in samples of purified theranosomes or in cell lysates was determined by fluorescence spectroscopy. An SLM Aminco Bowman Series 2 luminescence spectrometer was used, and the excitation wavelength was 410 nm. The drug concentration was obtained from fluorescence emission data based on a standard concentration curve of m-THPC. For m-THPC quantification in theranosomes, Triton X-100 was added at 0.3% final concentration in order to lyse theranosomes.

Iron Quantification. Iron quantification was carried out by electron spin resonance spectrometry (Varian E102; Agilent Technology, Massy, France) operating at 9.26 GHz. For the analysis, 2 μL of theranosome suspension (25 μM of m-THPC) was used. The iron concentration in the sample was calculated from the electron spin resonance absorption.

Confocal Microscopy. The PKH67-stained (in green) theranosomes were incubated with TC-1 cells seeded on glass lamellae. After 2 or 18 h of incubation, treated cells and controls were fixed in 4% paraformaldehyde solution and their nuclei were stained by Dapi (Sigma) following the manufacturer's instructions. Cells were observed by an Olympus JX81/BX61 device/Yokogawa CSU device spinning disk microscope (Andor Technology plc, Belfast, Northern Ireland), equipped with a 60× Plan-ApoN oil objective lens (60×/1.42 oil, Olympus). The PKH67 green was excited with an air-cooled ion laser at 488 nm, and fluorescence emission was collected with a filter at 525 nm. For both m-THPC and Dapi, the excitation wavelength was 405 nm, while fluorescence emission was collected with filters at 685 and 445 nm, respectively.

***In Vitro* Photodynamic Therapy.** The PC3, SKOV-3, and TC-1 cells were seeded in 24-well plates and incubated overnight at 37 °C in a humidified 5% CO_2 atmosphere. After PBS rinsing, the cells were incubated with 250 μL of theranosomes or m-THPC at 0.1 or 0.5 μM for 2 h in the dark at 37 °C in a humidified 5% CO_2 atmosphere. After that, cells were rinsed and incubated for 24 h before laser exposure. Wells were irradiated individually using a 650 nm diode laser featuring a fiber delivery system (BWT) at a light fluence of 10 J/cm^2 (100 mW/cm^2 for 100 s). At this wavelength, there is a lower attenuation of the excitation light when compared to 400 nm. Cells were incubated for 24 h before cytotoxic assessment by the Alamar Blue test (Invitrogen), according to the supplier's instructions.

Animal Model and *in Vivo* Photodynamic Therapy. All animal experiments were performed in agreement with institutional animal use and care regulations after approval by the local Ethics Committee (register number CEEA34.AAS.013.12). Nude NMRI mice (8-week-old, female) were injected subcutaneously on the rear of both flanks with 5×10^5 TC-1 cancer cells suspended in PBS. When solid tumors reached about 130 mm^3, the animals were randomized into three groups ($n = 5$ tumors per group): m-THPC injected and light irradiated, theranosome injected and light irradiated, and untreated control group (no injection, no irradiation). Tumor size was estimated by measuring its orthogonal diameter using a caliper. The tumor volume (V) was calculated using $V = Dd^2/2$, where D is the longest diameter and d is the diameter perpendicular to D. The mean tumor size ± SEM (standard error of the mean) for theranosome, m-THPC, and control groups was 170.7 ± 52.60, 118.5 ± 21.97, and 144.9 ± 72.08 mm^3, respectively. There was no statistically significant difference comparing the tumor size between groups ($p > 0.5$). The m-THPC and theranosome groups were injected intratumorally with 50 μL of theranosomes or m-THPC (in a solution of ethanol/polyethylene glycol 400/water at a 2/3/5 volume ratio) both at a 25 μM drug concentration. After 20 h, animals from both groups were irradiated using a DIOMED 630 PDT laser at a fluence of 30 J/cm^2 (77 mW/cm^2 for 390 s, $\lambda = 630$ nm). Tumors were also irradiated 24 h later.

The day of the first irradiation was considered day 0. Tumor volume for all mice was followed until day 7 and normalized to the volume corresponding to day 0.

Histology. Tumor tissues were harvested from the mice 2 or 7 days after photodynamic therapy. Tissues were fixed in formalin, dehydrated in graded solutions of ethanol, and embedded in paraffin. Thin sections of 5 μm were stained with H & E, and 7 μm thick sections were stained with Perl's staining and counterstained with Nuclear Fast Red.

Statistics. Data are presented as standard deviation from the mean or as standard error of the mean ($n = 3$ or $n = 5$). Student's t test was performed to determine a significant difference between the test and control groups using the Prism 3.0 version of GraphPad software (USA). A minimum of 95% confidence level was considered significant. *, **, and *** indicates $p < 0.05$, $p < 0.01$, and $p < 0.001$, respectively, *versus* control.

Conflict of Interest: The authors declare no competing financial interest.

Supporting Information Available: Additional figures and supplementary references. This material is available free of charge *via* the Internet at http://pubs.acs.org.

Acknowledgment. This work was supported by the European project Magnifyco (Contract NMP4-SL-2009-228622). The authors thank Gwennhael Autret and the Small Animal Imaging Platform Paris–Descartes PARCC-HEGP for MRI, and Small Animal Imaging Platform Paris–Descartes Faculty of Pharmacy for fluorescence imaging. We are grateful to Professor Patrick Bruneval for anatomopathological advice and Christine Longin and Sophie Chat from Mima2 platform–Inra (Jouy en Josas) for TEM analysis. J.K.-T. was supported by the grant from the European network ENCITE. ImageStream^X equipment on the platform ImagoSeine (IJM, University Paris Diderot) was supported by the Region Ile de France (contract no. E539). We also acknowledge Geneviève Bourg-Heckly for fruitful discussions and for providing the Diomed 630 PDT laser.

REFERENCES AND NOTES

1. Sanhai, W. R.; Sakamoto, J. H.; Canady, R.; Ferrari, M. Seven Challenges for Nanomedicine. *Nat. Nanotechnol.* **2008**, *3*, 242–244.
2. Dobrovolskaia, M. A.; McNeil, S. E. Immunological Properties of Engineered Nanomaterials. *Nat. Nanotechnol.* **2007**, *2*, 469–478.
3. Wattendorf, U.; Merkle, H. P. PEGylation as a Tool for the Biomedical Engineering of Surface Modified Microparticles. *J. Pharm. Sci.* **2008**, *97*, 4655–4669.
4. Ratajczak, J.; Wysoczynski, M.; Hayek, F.; Janowska-Wieczorek, A.; Ratajczak, M. Membrane-Derived Microvesicles: Important and Underappreciated Mediators of Cell-to-Cell Communication. *Leukemia* **2006**, *20*, 1487–1495.
5. Boulanger, C. M.; Amabile, N.; Tedgui, A. Circulating Microparticles: A Potential Prognostic Marker for Atherosclerotic Vascular Disease. *Hypertension* **2006**, *48*, 180–186.
6. Piccin, A.; Murphy, W. G.; Smith, O. P. Circulating Microparticles: Pathophysiology and Clinical Implications. *Blood Rev.* **2007**, *21*, 157–171.
7. Skog, J.; Würdinger, T.; Van Rijn, S.; Meijer, D. H.; Gainche, L.; Curry, W. T.; Carter, B. S.; Krichevsky, A. M.; Breakefield, X. O. Glioblastoma Microvesicles Transport RNA and Proteins that Promote Tumour Growth and Provide Diagnostic Biomarkers. *Nat. Cell Biol.* **2008**, *10*, 1470–1476.
8. van Dommelen, S. M.; Vader, P.; Lakhal, S.; Kooijmans, S. A. A.; van Solinge, W. W.; Wood, M. J. A.; Schiffelers, R. M. Microvesicles and Exosomes: Opportunities for Cell-Derived Membrane Vesicles in Drug Delivery. *J. Controlled Release* **2012**, *161*, 635–644.
9. Yoo, J. W.; Irvine, D. J.; Discher, D. E.; Mitragotri, S. Bio-inspired, Bioengineered and Biomimetic Drug Delivery Carriers. *Nat. Rev. Drug Discovery* **2011**, *10*, 521–535.
10. Alvarez-Erviti, L.; Seow, Y.; Yin, H. F.; Betts, C.; Lakhal, S.; Wood, M. J. A. Delivery of SiRNA to the Mouse Brain by Systemic Injection of Targeted Exosomes. *Nat. Biotechnol.* **2011**, *29*, 341–345.
11. Sun, D.; Zhuang, X.; Xiang, X.; Liu, Y.; Zhang, S.; Liu, C.; Barnes, S.; Grizzle, W.; Miller, D.; Zhang, H. G. A Novel Nanoparticle Drug Delivery System: The Anti-Inflammatory Activity of Curcumin Is Enhanced When Encapsulated in Exosomes. *Mol. Ther.* **2010**, *18*, 1606–1614.
12. Amstad, E.; Kohlbrecher, J.; Müller, E.; Schweizer, T.; Textor, M.; Reimhult, E. Triggered Release from Liposomes through Magnetic Actuation of Iron Oxide Nanoparticle Containing Membranes. *Nano Lett.* **2011**, *11*, 1664–1670.
13. Guardia, P.; Di Corato, R.; Lartigue, L.; Wilhelm, C.; Espinosa, A.; Garcia-Hernandez, M.; Gazeau, F.; Manna, L.; Pellegrino, T. Water-Soluble Iron Oxide Nanocubes with High Values of Specific Absorption Rate for Cancer Cell Hyperthermia Treatment. *ACS Nano* **2012**, *6*, 3080–3091.
14. Daldrup-Link, H. E.; Golovko, D.; Ruffell, B.; DeNardo, D. G.; Castaneda, R.; Ansari, C.; Rao, J.; Tikhomirov, G. A.; Wendland, M. F.; Corot, C. MRI of Tumor-Associated Macrophages with Clinically Applicable Iron Oxide Nanoparticles. *Clin. Cancer Res.* **2011**, *17*, 5695–5704.
15. Long, C. M.; Bulte, J. W. M. *In Vivo* Tracking of Cellular Therapeutics Using Magnetic Resonance Imaging. *Expert Opin. Biol. Ther.* **2009**, *9*, 293–306.
16. Senge, M. O.; Brandt, J. C. Temoporfin (Foscan®, 5, 10, 15, 20 Tetra (m-hydroxyphenyl chlorin)–A Second Generation Photosensitizer. *Photochem. Photobiol.* **2011**, *87*, 1240–1296.
17. Wilhelm, C.; Gazeau, F. Universal Cell Labelling with Anionic Magnetic Nanoparticles. *Biomaterials* **2008**, *29*, 3161–3174.
18. Luciani, N.; Wilhelm, C.; Gazeau, F. The Role of Cell-Released Microvesicles in the Intercellular Transfer of Magnetic Nanoparticles in the Monocyte/Macrophage System. *Biomaterials* **2010**, *31*, 7061–7069.
19. Hugel, B.; Martínez, M. C.; Kunzelmann, C.; Freyssinet, J.-M. Membrane Microparticles: Two Sides of the Coin. *Physiology* **2005**, *20*, 22–27.
20. Al-Nedawi, K.; Meehan, B.; Micallef, J.; Lhotak, V.; May, L.; Guha, A.; Rak, J. Intercellular Transfer of the Oncogenic Receptor EGFRvIII by Microvesicles Derived from Tumour Cells. *Nat. Cell Biol.* **2008**, *10*, 619–624.
21. Dolo, V.; D'Ascenzo, S.; Violini, S.; Pompucci, L.; Festuccia, C.; Ginestra, A.; Vittorelli, M. L.; Canevari, S.; Pavan, A. Matrix-Degrading Proteinases Are Shed in Membrane Vesicles by Ovarian Cancer Cells *in Vivo* and *in Vitro*. *Clin. Exp. Metastasis* **1999**, *17*, 131–140.
22. Kim, C. W.; Lee, H. M.; Lee, T. H.; Kang, C.; Kleinman, H. K.; Gho, Y. S. Extracellular Membrane Vesicles from Tumor Cells Promote Angiogenesis *via* Sphingomyelin. *Cancer Res.* **2002**, *62*, 6312–6317.
23. Al-Nedawi, K.; Meehan, B.; Kerbel, R. S.; Allison, A. C.; Rak, J. Endothelial Expression of Autocrine VEGF upon the Uptake of Tumor-Derived Microvesicles Containing Oncogenic EGFR. *Proc. Natl. Acad. Sci. U.S.A.* **2009**, *106*, 3794–3799.
24. Kim, J. W.; Wieckowski, E.; Taylor, D. D.; Reichert, T. E.; Watkins, S.; Whiteside, T. L. Fas Ligand-Positive Membranous Vesicles Isolated from Sera of Patients with Oral Cancer Induce Apoptosis of Activated T Lymphocytes. *Clin. Cancer Res.* **2005**, *11*, 1010–1020.
25. Valenti, R.; Huber, V.; Iero, M.; Filipazzi, P.; Parmiani, G.; Rivoltini, L. Tumor-Released Microvesicles as Vehicles of Immunosuppression. *Cancer Res.* **2007**, *67*, 2912–2915.
26. Safaei, R.; Larson, B. J.; Cheng, T. C.; Gibson, M. A.; Otani, S.; Naerdemann, W.; Howell, S. B. Abnormal Lysosomal Trafficking and Enhanced Exosomal Export of Cisplatin in Drug-Resistant Human Ovarian Carcinoma Cells. *Mol. Cancer Ther.* **2005**, *4*, 1595–1604.
27. Gong, J.; Jaiswal, R.; Mathys, J. M.; Combes, V.; Grau, G.; Bebawy, M. Microparticles and their Emerging Role in Cancer Multidrug Resistance. *Cancer Treat. Rev.* **2012**, *38*, 226–234.
28. Castellana, D.; Zobairi, F.; Martinez, M. C.; Panaro, M. A.; Mitolo, V.; Freyssinet, J. M.; Kunzelmann, C. Membrane Microvesicles as Actors in the Establishment of a Favorable

Prostatic Tumoral Niche: A Role for Activated Fibroblasts and CX3CL1-CX3CR1 Axis. *Cancer Res.* **2009**, *69*, 785–793.
29. Janowska-Wieczorek, A.; Wysoczynski, M.; Kijowski, J.; Marquez-Curtis, L.; Machalinski, B.; Ratajczak, J.; Ratajczak, M. Z. Microvesicles Derived from Activated Platelets Induce Metastasis and Angiogenesis in Lung Cancer. *Int. J. Cancer* **2005**, *113*, 752–760.
30. Janowska-Wieczorek, A.; Marquez-Curtis, L. A.; Wysoczynski, M.; Ratajczak, M. Z. Enhancing Effect of Platelet-Derived Microvesicles on the Invasive Potential of Breast Cancer Cells. *Transfusion* **2006**, *46*, 1199–1209.
31. Tesselaar, M.; Romijn, F.; Van Der Linden, I.; Prins, F.; Bertina, R.; Osanto, S. Microparticle-Associated Tissue Factor Activity: A Link between Cancer and Thrombosis?. *J. Thromb. Haemost.* **2007**, *5*, 520–527.
32. Muralidharan-Chari, V.; Clancy, J. W.; Sedgwick, A.; D'Souza-Schorey, C. Microvesicles: Mediators of Extracellular Communication during Cancer Progression. *J. Cell Sci.* **2010**, *123*, 1603–1611.
33. Wang, S.; Kim, G.; Lee, Y.-E. K.; Hah, H. J.; Ethirajan, M.; Pandey, R. K.; Kopelman, R. Multifunctional Biodegradable Polyacrylamide Nanocarriers for Cancer Theranostics—A "See and Treat" Strategy. *ACS Nano* **2012**, *6*, 6843–6851.
34. Chen, Z.; Penet, M.-F.; Nimmagadda, S.; Li, C.; Banerjee, S. R.; Winnard, P. T.; Artemov, D.; Glunde, K.; Pomper, M. G.; Bhujwalla, Z. M. PSMA-Targeted Theranostic Nanoplex for Prostate Cancer Therapy. *ACS Nano* **2012**, *6*, 7752–7762.
35. Al-Jamal, W. T.; Kostarelos, K. Liposomes: From a Clinically Established Drug Delivery System to a Nanoparticle Platform for Theranostic Nanomedicine. *Acc. Chem. Res.* **2011**, *44*, 1094–1104.
36. Chang, H.-I.; Yeh, M.-K. Clinical Development of Liposome-Based Drugs: Formulation, Characterization, and Therapeutic Efficacy. *Int. J. Nanomed.* **2012**, *7*, 49–60.
37. Maherani, B.; Arab-Tehrany, E. R.; Mozafari, M.; Gaiani, C.; Linder, M. Liposomes: A Review of Manufacturing Techniques and Targeting Strategies. *Curr. Nanosci.* **2011**, *7*, 436–452.
38. Silva, A. K. A.; Di Corato, R.; Gazeau, F.; Pellegrino, T.; Wilhelm, C. Magnetophoresis at the Nanoscale: Tracking the Magnetic Targeting Efficiency of Nanovectors. *Nanomedicine* **2012**, *7*, 1713–1727.